Tautomeric Mixture Coordination Enables Efficient Lead-Free Perovskite LEDs

Ning Wang (ningwang@jlu.edu.cn)
Jilin University https://orcid.org/0000-0001-9570-952X

Dongyuan Han
Jilin University

Jie Wang
Jilin University

Lorenzo Agosta
École Polytechnique Fédérale de Lausanne (EPFL)

Ziang Zang
Jilin University

Bin Zhao
Jilin University

Lingmei Kong
Shanghai University

Haizhou Lu
EPFL https://orcid.org/0000-0001-9692-7860

Irea Mosquera-Lois
EPFL

Virginia Carnevali
École Polytechnique Fédérale de Lausanne (EPFL) https://orcid.org/0000-0002-8905-2928

Jianchao Dong
Jilin University

Jianheng Zhou
Jilin University

Huiyu Ji
Jilin University

Lukas Pfeifer
École Polytechnique Fédérale de Lausanne https://orcid.org/0000-0002-8461-3909

Shaik Zakeeruddin
Ecole Polytechnique Federale de Lausanne

Yingguo Yang
Shanghai Institute of Applied Physics https://orcid.org/0000-0002-1749-2799

Bo Wu

South China Normal University

Ursula Rothlisberger

Ecole Polytechnique Fédérale de Lausanne https://orcid.org/0000-0002-1704-8591

Xuyong Yang

Shanghai University https://orcid.org/0000-0003-3597-1491

Michael Graetzel

École Polytechnique Fédérale de Lausanne https://orcid.org/0000-0002-0068-0195

Physical Sciences - Article

Keywords:

Posted Date: January 19th, 2023

DOI: https://doi.org/10.21203/rs.3.rs-2465931/v1

Additional Declarations: There is **NO** Competing Interest.

Version of Record: A version of this preprint was published at Nature on August 9th, 2023. See the published version at https://doi.org/10.1038/s41586-023-06514-6.

Tautomeric Mixture Coordination Enables Efficient Lead-Free Perovskite LEDs

Dongyuan Han[1#], Jie Wang[1#], Lorenzo Agosta[2], Ziang Zang[1], Bin Zhao[1], Lingmei Kong[3], Haizhou Lu[4,5]*, Irea Mosquera-Lois[2], Virginia Carnevali[2], Jianchao Dong[1], Jianheng Zhou[1], Huiyu Ji[1], Lukas Pfeifer[4], Shaik M. Zakeeruddin[4], Yingguo Yang[6,7], Bo Wu[8], Ursula Rothlisberger[2], Xuyong Yang[3]*, Michael Grätzel[4]*, Ning Wang[1]*

[1]College of Physics, Jilin University, Changchun, China.
[2]Laboratory of Computational Chemistry and Biochemistry, Institute of Chemical Sciences and Engineering, École Polytechnique Fédérale de Lausanne (EPFL), Lausanne, Switzerland.
[3]Key Laboratory of Advanced Display and System Applications of Ministry of Education, Shanghai University, Shanghai, China.
[4]Laboratory of Photonics and Interfaces, Institute of Chemical Sciences and Engineering, École Polytechnique Fédérale de Lausanne (EPFL), Lausanne, Switzerland.
[5]SEU-FEI Nano-Pico Center, Key Laboratory of MEMS of Ministry of Education, School of Electronics Science and Engineering, Southeast University, Nanjing, China.
[6]Shanghai Synchrotron Radiation Facility (SSRF), Zhangjiang Lab, Shanghai Advanced Research Institute, Chinese Academy of Sciences, Shanghai, China.
[7]School of Microelectronics, Fudan University, Shanghai, China.
[8]Guangdong Provincial Key Laboratory of Optical Information Materials and Technology and Institute of Electronic Paper Displays, South China Academy of Advanced Optoelectronics, South China Normal University, Guangzhou, China.

[#]These authors contributed equally to this work.
*Correspondence to: haizhou.lu@epfl.ch; yangxy@shu.edu.cn; michael.graetzel@epfl.ch; ningwang@jlu.edu.cn.

Abstract

Lead (Pb) halide perovskite light-emitting diodes (PeLEDs) have demonstrated extraordinary optoelectronic performance[1-3]. However, the toxicity of Pb has raised as a serious concern[4,5]. Removing Pb from the best-performing PeLEDs without compromising their excellent external quantum efficiencies (EQEs) remains a challenge. Here we report a tautomeric mixture coordination-induced electron localization strategy to fundamentally stabilize Pb-free TEA_2SnI_4 (TEAI, 2-thiophenethylammonium iodide) perovskite by incorporating cyanuric acid (CA). We demonstrate that a crucial function of the coordination is to amplify electronic effects and even extend to Sn atoms without strong bonding with CA, due to the formation of H-bonded tautomeric dimer and trimer superstructures on the perovskite surface. This electron localization weakens adverse effects from Anderson localization and contributes to more ordered and stable crystal structure in the resultant TEA_2SnI_4, which synergistically improve the perovskite with two orders of magnitude reduction in nonradiative recombination capture coefficient and about 2-fold enhancement in exciton binding energy. Levering by the interactional profit, our target Pb-free PeLED demonstrated an EQE of up to 20.13 per cent, representing a performance comparable to that of state-of-the-art Pb-containing PeLEDs[6-8]. We anticipate that these findings will provide insights into the stabilization of Sn(II) perovskites and inspire researchers to pioneer Pb-free perovskite applications.

Main text

Metal halide perovskites have recently attracted great attention as light emitters because of their adjustable emission wavelength, wide color gamut, low-cost solution processing and high photoluminescence quantum yield (PLQY), making them promising candidates for the next-generation display and information technologies[9-12]. The high-performance PeLEDs with EQEs of > 20% are invariably based on Pb-containing perovskite compositions[1,6,9]. However, the toxicity of Pb in PeLEDs may limit their future implementations[13]. Exploration of highly efficient and stable Pb-free perovskite-based light emitters has been an urgent research topic, and Sn-based perovskite has been regarded as a promising candidate because Sn has a similar valence electron configuration and ionic radius as Pb[14,15]. Nonetheless, the endsville EQEs of Sn-based PeLEDs are seriously lagging behind those of Pb-based counterparts[16-18]. Most strategies adopted to improve Sn-based PeLEDs have been focusing on inhibiting the oxidation of Sn^{2+} by introducing Sn compensators[19] and reducing agents[20]. Unfortunately, only limited improvement has been achieved because those techniques cannot effectively suppress the defects in the resultant Sn perovskite films. Furthermore, the residual chemical agents often destroy the orderliness of the crystal lattice of Sn perovskites, resulting in Anderson localization[21], which is detrimental to the optoelectronic properties. Morphological control[18] and solvent engineering[17] methods have also been developed to increase the EQE of Sn-based PeLEDs of up to 5.4%. The low EQE of Sn-PeLEDs implies a limited understanding of the intrinsic instability of Sn^{2+}, and more in-depth studies are needed to further enhance both EQE and stability of Sn-based PeLEDs.

The facile oxidation of Sn^{2+} fundamentally originates from the delocalized $5s^2$ lone pair electrons, which can cause detrimental p-type self-doping[13,22]. Recently, Sargent *et al*.[16] demonstrated a chemical coordination strategy to reduce Sn^{4+} that successfully boosted both EQE (up to 5%) and stability of Sn-based PeLEDs. In addition, Ye *et al*.[23] reported localized electron engineering for improving Sn-based perovskite solar cells. We were then motivated to establish a strong chemical coordination with Sn^{2+} to inhibit electron delocalization, boosting Sn-based PeLEDs. CA is a typical delocalized aromatic compound which possesses low electronegativity and strong electron-donating ability[24,25], favoring the interaction with Sn^{2+}. Importantly, ab-initio molecular dynamics (AIMD) simulations show that a mixture of CA tautomers is key to form strong chemical bonds on the Sn perovskite surface.

To understand the chemical coordination interaction between CA and two-dimensional TEA_2SnI_4 perovskite, we performed Fourier transform infrared spectroscopy (FTIR) measurements. Fig. 1a and Supplementary Fig. 1 show that the stretching vibration of C=N at 1678 cm^{-1} for CA molecule shifted to 1697 cm^{-1} for the CA-treated Sn perovskite, suggesting a strong C=N bond, which arises from the interaction of C=N and Sn-perovskite. This is consistent with the electrostatic potential of the enol form of the CA molecule (Extended Data Fig. 1), indicating that the region near nitrogen atom in the triazine ring has a high electron density. It could act as the footstone for donating lone-pair electrons to coordinate with Sn(II)[26]. The appearance of the characteristic vibration peak of C=O at 1775 cm^{-1} for CA and CA-treated Sn perovskite implies the co-existence of keto form, i.e., the presence of a tautomeric mixture of CA, which will be discussed later.

Subsequently, ^1H nuclear magnetic resonance (NMR) measurements were carried out. Chemical shift of the resonance signal of CA (Fig.1b) indicates the formation of hydrogen bonds in the form of N=C-OH$\cdots I^-$[16]. The broad resonance signal of SnI_2-CA suggests that CA molecule is immobilized by the N=C-OH$\cdots I^-$ hydrogen bonds, which prevents the migration of

I^-. Similar phenomenon was also observed in ^{13}C NMR spectroscopy, which further confirms the strong interaction between CA and Sn(II). The FTIR and NMR results agreed well with X-ray photoelectron spectroscopy (XPS) measurements (Supplementary Fig. 2), which show chemical shift of the Sn 3*d* and I 3*d* XPS peaks after introducing CA into the Sn perovskite.

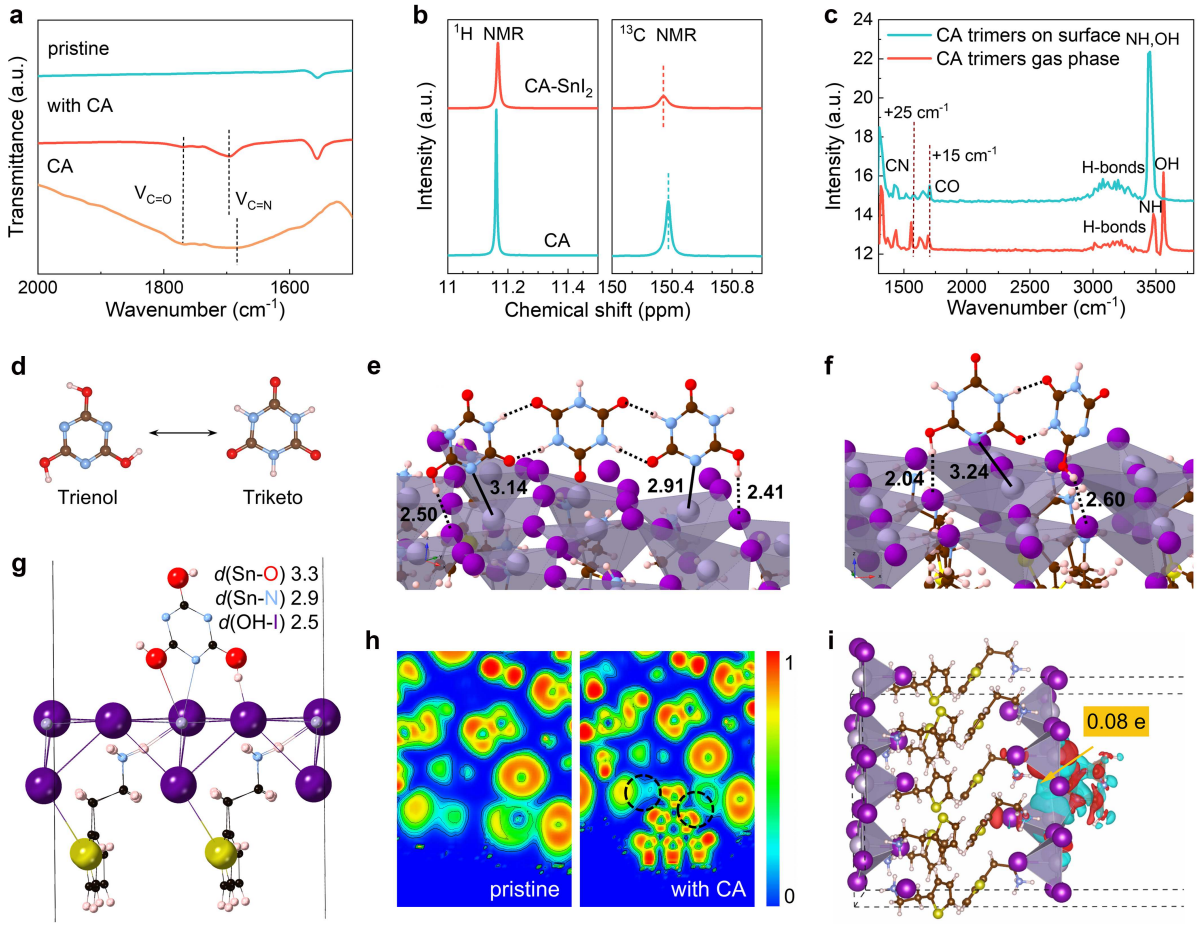

Fig. 1 | Interaction and configuration between CA and TEA_2SnI_4 perovskite. a, FTIR spectra of the TEA_2SnI_4 with and without CA, and the pure CA. **b**, ^1H NMR (left) and ^{13}C NMR (right) spectra for the pure CA and the composite of CA+SnI_2. **c**, Vibrational power spectra of the most stable trimer configuration in vacuum adsorbed on the perovskite surface. **d**, Trienol and triketo forms of CA. **e**, **f**, The most stable configurations for the tautomeric CA dimer (**e**) and trimer (**f**) bonded to the Sn perovskite surface. The distances are in Å. Color code: Sn in grey, I in purple, S in yellow, C in brown, H in pink, O in red, N in blue. **g**, Configuration and characteristic interactions of CA on the TEA_2SnI_4 perovskite surface. Color code: Sn in grey, I in purple, S in yellow, C in black, H in pink, O in red, N in blue. **h**, ELF images of the pristine and the perovskite with CA, which were obtained in systems with an iodide vacancy. **i**, Charge density difference between the Sn perovskite and CA.

AIMD simulations were employed to investigate the configuration of CA on the perovskite surface, we observed the formation of CA dimers and trimers consisting of mixed enol and keto forms (Extended Data Fig. 2). In fact, the possibility of a strong C=N···Sn^{2+} coordination of the enol form leads to a partial surface-induced tautomerization of the thermodynamically more stable keto form. This tautomeric mixture is stabilized by the strong intermolecular N-H···O/O-H···N hydrogen bonds[27,28]. We also carried out a computation of the vibrational spectra of various types of surface-absorbed CA molecules (Fig.1c). When the trimer is adsorbed on the surface, a blue shift of 25 cm^{-1} and 15 cm^{-1} (with respect to the same isolated trimer) is presented for C-N (1650 cm^{-1}) and C-O (1775 cm^{-1}) stretch vibrations, which is in

good agreement with the experimental FTIR measurements. We note the presence of O-H vibrational modes at 2900~3300 cm^{-1} is consistent with the formation of strong H-bonds, a signature of the keto-enol H-bonded di/trimeric forms.

We conclude that CA molecules on the Sn perovskites are composed of a mixture of keto and enol tautomers that form dimers/trimers (Supplementary Table 1). These ordered complexes are nearly commensurate with the perovskite lattice (Sn···Sn second nearest distance is 1.05 nm while the O-C-N···O-C-N distance of the extreme CA molecules in the trimer is 1.1 nm) allowing for strong N-Sn coordination augmented by the interaction between OH-I^- and H-bond (Figs. 1d-1g), providing an efficacious protection of the perovskite surface against Sn(II) oxidation as well as Sn and I^- loss. Beyond surface passivation/protection, the polyfunctional character of CA in combination with its ability to form ordered structures with a well-defined perpendicular orientation of the aromatic ring planes with respect to the surface suggest an additional potential to stabilize grain boundaries by crosslinking different grains through N/O-Sn and H-I interaction. Noticeably, this unique interaction between CA and Sn perovskite is distinctly different from previous reports (Extended Data Fig. 2)[1,16].

To understand how CA could stabilize the Sn perovskite, a Bader analysis was performed. It was found that the Sn electron density becomes more localized upon coordination substantially reducing the corresponding Bader volume from 59~62 au^3 to 24 au^3. This effect even extends to nearby surface Sn^{2+} atoms that have only weak interaction with CA (d(Sn-O) = 3.3 Å, d(Sn-N) = 3.3 Å), and still experience a clear localization of the Sn charge density (Bader volume of 45~56 au^3). Both the coordinating bonds and their localizing effect contribute to the stabilization of surface Sn^{2+} thus preventing Sn(II) oxidation.

In addition, the electron localization function (ELF) was calculated to provide a mapping of electron cloud in the pristine and the CA-treated Sn perovskite (Fig. 1h). The electron cloud in the dashed region of the CA-treated Sn perovskite indicates strong electron localization of Sn^{2+}. The triketone form of CA also showed similar property (Extended Data Fig. 1). The effect of CA on electronic properties is further investigated by applying charge density difference (Fig. 1i). Electron transfer between CA and Sn perovskite is evaluated to be 0.08 e, suggesting strong interaction between CA and undercoordinated Sn^{2+}, which inhibits charge transfer from Sn^{2+} to O_2 molecule (Supplementary Table 2)[29-31]. The planar-averaged charge density difference (Extended Data Fig. 1 and Supplementary Fig. 3) also proves the charge redistribution at the interface, which can benefit the carrier transport and improve electrical conductivity. Decreased dielectric coefficient confirmed the improved electrical conductivity.

Scanning electron microscope (SEM) images of the TEA_2SnI_4 perovskite with 5% CA showed a smoother surface morphology than the other sample (Extended Data Fig. 3 and Supplementary Fig. 4). Atomic force microscope (AFM) images further manifest the flatter film surface in the treated sample. Grazing incidence wide-angle X-ray scattering (GIWAXS) measurements (Fig. 2a, Extended Data Fig. 4 and Supplementary Fig. 5) suggested a highly uniform parallel orientation of the Sn perovskite films[32,33]. Compared with the pristine, the target film showed a higher prefer-orientation, stronger diffraction intensity and narrower full width at half maximum (FWHM), which implies much more ordered stacking and better crystallinity of perovskite crystal plates due to the introduction of CA, therefore avoiding Anderson localization[34]. Moreover, the low-n phases components of the Sn perovskite films are suppressed effectively with the CA treatment. Such preferentially oriented crystallinity favors efficient carrier injection and prevents ion migration along the vertical direction during device operation[35].

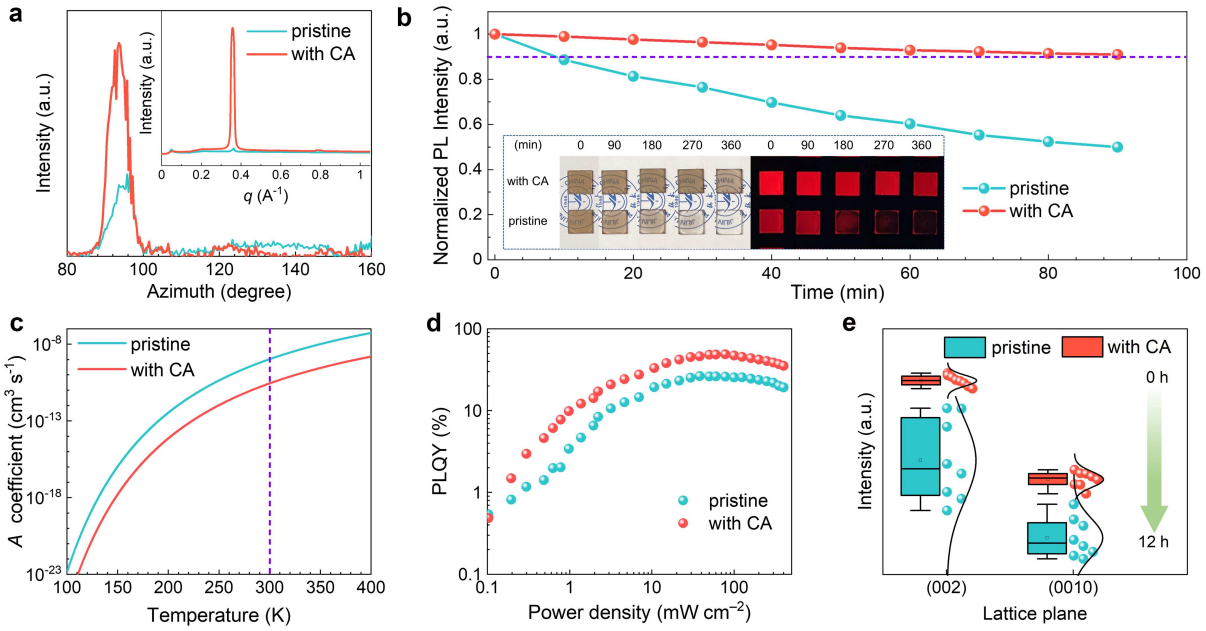

Fig. 2 | Crystallization kinetics and nonradiative recombination evaluation. a, Intensity curves of GIWAXS patterns along the (002) ring for the samples with and without CA. Inset, integrated intensity of GIWAXS patterns for the samples. **b**, Time-dependent normalized PL intensity measurements for the pristine and the TEA_2SnI_4 film with CA exposed to dry air (20% humidity, RT) for 90 min. Inset, photographs of the samples in air and in dark with an excitation wavelength of 365 nm. **c**, Curves of nonradiative capture coefficients *A* versus temperature of the Sn perovskites. **d**, Excitation-intensity-dependent PLQYs of the Sn perovskite films with and without CA. **e**, Stability of XRD measurements of the pristine and the sample with CA for 12 hours in dry air.

Kelvin probe force microscopy measurements revealed that the Sn perovskite film with CA possesses a higher surface potential (Extended Data Fig. 3 and Supplementary Fig. 6), which is mainly due to the reduced number of surface defects[36]. Calculations of density of states (Extended Data Fig. 1) showed that iodide vacancy states in the band edge of the Sn perovskite were reduced by CA[37], avoiding the presence of undercoordinated Sn^{2+} that aggravates Sn^{2+} oxidation. The suppression of I defects is vital to avoid nonradiative recombination loss in Sn perovskites. We find that the content of I^- substantially increases from 82.4% in the pristine to 97.1% in the treated film (Extended Data Fig. 5 and Supplementary Table 3). The Sn/I ratio in the pristine and the target film were calculated to be 0.25 and 0.23, respectively. These results indicate that CA can prevent the migration of I^- and suppress its evolution to I_2 or I_3^-[38]. Further, we find that the content of Sn is increased by a factor of 1.09 compared to the pristine. Beyond suppressing I and Sn loss, CA prevents Sn^{2+} oxidation, as demonstrated by XPS measurements, which illustrates a decrease in the content of Sn^{4+} from 16.5% in the pristine to 7.6% in the target sample (Extended Data Fig. 5). To elucidate the effect of CA on trap states, we carried out measurements on Urbach energy (E_U) and time-resolved photoluminescence (TRPL) spectroscopy (Extended Data Fig. 6). The E_U value decreased from 137 meV to 85 meV and the average carrier lifetime increased from 1.44 ns to 3.45 ns when CA was introduced. Besides, enhanced photoluminescence (PL) intensity is also observed in the CA-treated film.

Generally, the facile oxidation of Sn^{2+} to Sn^{4+} and the unstable crystal structures are responsible for undermining the stability of Sn perovskite films[29]. To check the shelf stability of the Sn perovskites in ambient air condition, time-dependent normalized PL measurements were performed (Fig. 2b and Supplementary Figs. 7 and 8). In contrast to the sharp reduction of PL

intensity of the pristine with time, the target film retained its 90% initial PL intensity within 90 min. It was further revealed that the nonradiative recombination capture coefficient A of the Sn perovskite sample was reduced by more than two orders of magnitude from 1.01×10^{-9} cm^3 s^{-1} to 2.45×10^{-11} cm^3 s^{-1} by introducing CA (Fig. 2c, Extended Data Fig. 6 and Supplementary Fig. 9). This indicates that the CA-treated Sn perovskite is potentially an excellent luminescent material. Excitation-intensity-dependent PLQY measurements showed that the PLQYs of the films increase with the excitation intensity to a large extent (Fig. 2d). It is well understood that, as the defect states are gradually filled, radiative bimolecular recombination begins to dominate the luminescence process during this test[39]. Afterwards, X-ray diffraction (XRD) characterization was carried out, and the patterns of the films with CA displayed stronger diffraction intensity and narrower FWHM (Extended Data Fig. 4), which are in contrast with the pristine. Furthermore, the XRD patterns of the films stored in dry air without encapsulation for different time are also presented for detecting the effect of CA on crystal structure of the Sn perovskites (Fig. 2e and Supplementary Fig. 10). After 720-minute storage, the diffraction intensity (002) of the films with CA decreases less than the pristine. The reduced non-radiative recombination coefficient and stabilized crystal structure act together to improve the Sn perovskite stability.

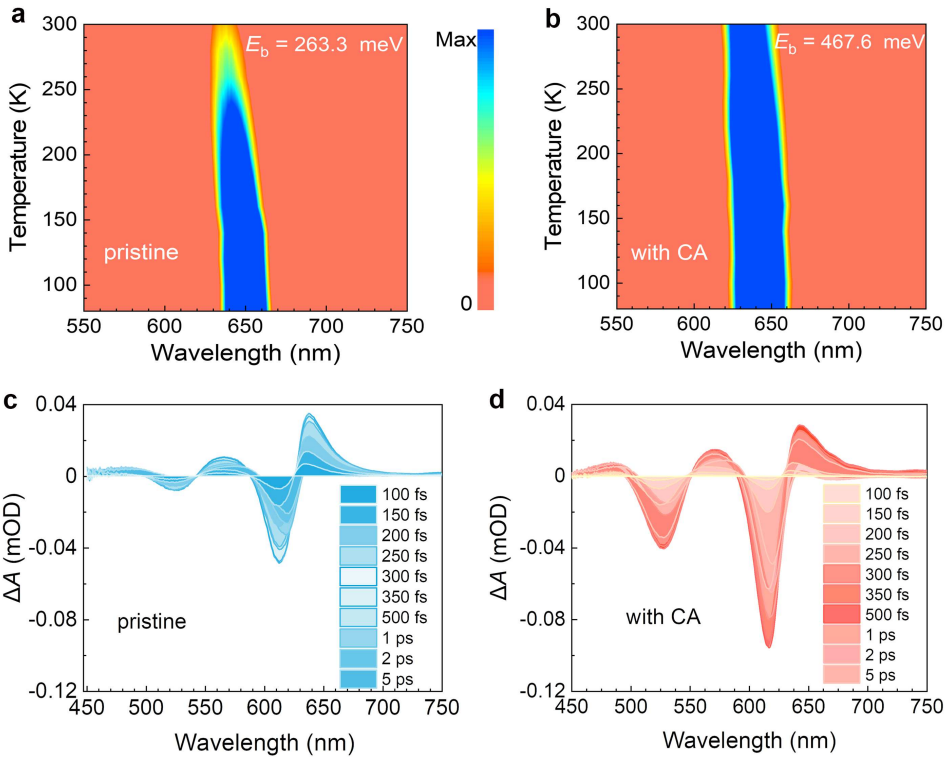

Fig. 3 | Photophysics and carrier dynamics of TEA_2SnI_4 films. a, **b**, Temperature-dependent PL spectra mapping for the pristine (**a**) and the Sn perovskite film with CA (**b**). **c**, **d**, TA spectra for the pristine (**c**) and the Sn perovskite film with CA (**d**).

As temperature increases (Figs. 3a and 3b), for the temperature-dependent steady-state PL spectra measurements, the PL intensity of the target film showed slightly decrease and the corresponding peak position blue shifted by ~5 nm comparing with the pristine (16 nm). These results indicate that the thermal quenching of fluorescence caused by nonradiative recombination is essentially inhibited in the target film through CA coordination[40]. We evaluated the exciton binding energy (E_b) of the target film to be 467.6 ± 43.3 meV, which is about two-fold higher than that (263.3 ± 30.1 meV) of the pristine (Extended Data Fig. 7). The enlarged E_b of the target film suggests a higher energy threshold for exciton dissociation, making them promising luminescent materials.

Transient absorption (TA) measurements revealed two pronounced photo-bleaching peaks at ~615 nm and ~522 nm for both the pristine and the target sample (Figs. 3c and 3d, Extended Data Fig. 7), respectively, which are attributed to the 1s and 2s excitons[41]. The enhanced TA signal at the two exciton resonances for the treated sample compared to the pristine (~4 times at 2s exciton and twice at 1s exciton) may be attributed to the enhanced Coulombic interaction and excitonic effect with CA treatment. We notice that within 5 ps after photoexcitation, the exciton bleaching peaks show fast redshift, which is usually recognized as the filling process of the band tail states. The smaller shift of transient bleach further confirmed the reduced band tail states in the treated sample. Furthermore, we analyzed the bleach recovery kinetics by fitting the decay curves with a tri-exponential function (Supplementary Fig. 11). The fast decay (τ_1) is attributed to the hot carrier relaxation, convoluted with the fast carrier trapping. The intermediate decay (τ_2) is responsible for the carrier trapping by defects. The treated sample shows a slower defect trapping rate, in agreement with reduced defect traps through CA coordination-induced electron localization. As a result, the bleach signal for the treated sample displays a higher fraction of long-lived component (slow decay $\tau_3 > 5$ ns) than that of the pristine (slow decay $\tau_3 > 4$ ns), which is attributed to the recombination of photoexcited species.

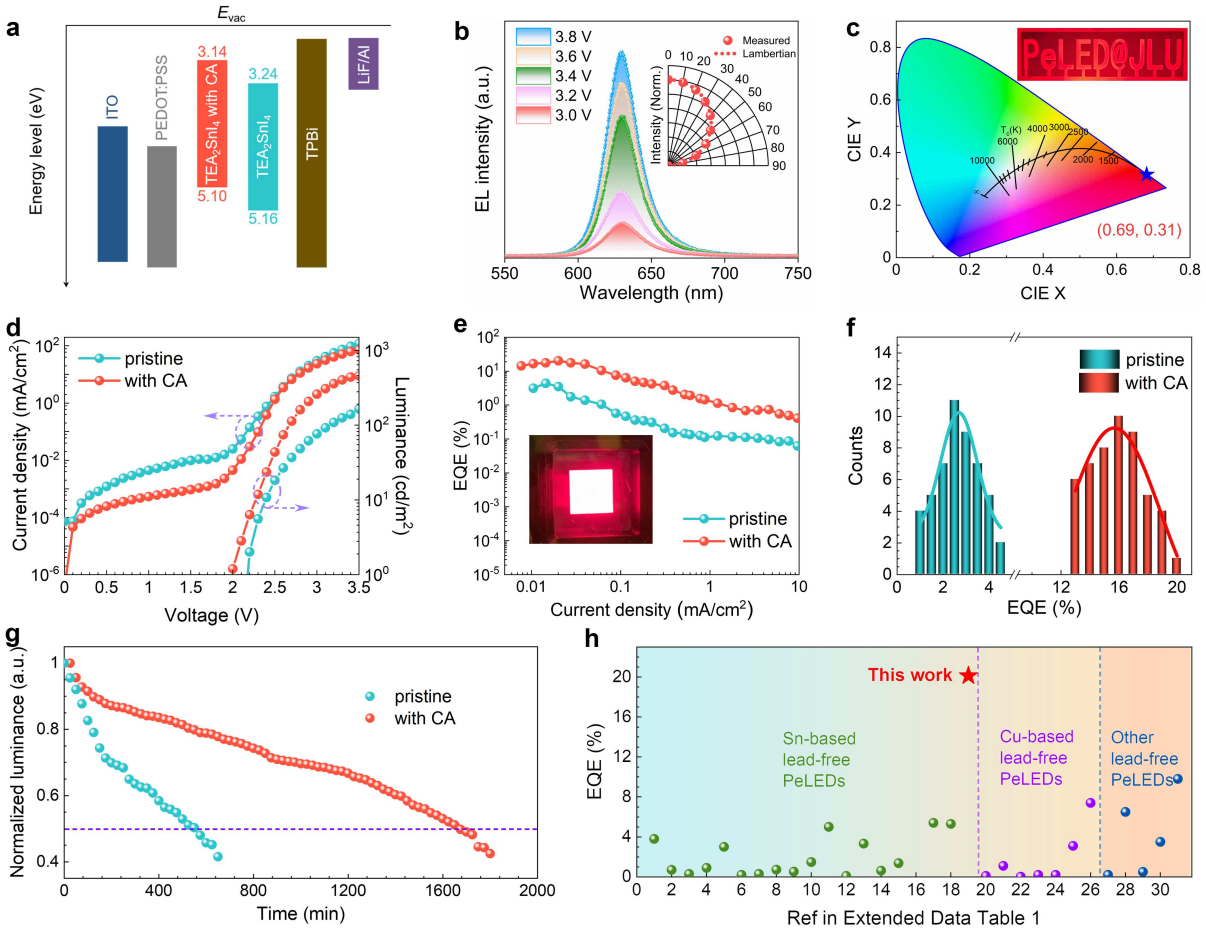

Fig. 4 | Device characterization. a, Energy level diagram of the devices used in this work. **b**, EL spectra of one target device with constant peak emission wavelength of 630 nm under different voltages. Inset, an angle-dependent EL intensity measurement. **c**, CIE color space plot of one target device. Inset, photograph of a lead-free PeLED with a pattern of 'PeLED@JLU'. **d**, *J-V-L* curves of the devices with and without CA. **e**, EQE curves of the devices with and without CA. Inset, photograph of a working device (effective area: 1.5 cm × 1.5 cm). **f**, Histograms of peak EQEs measured from 50 devices in one batch for the Sn-PeLEDs with and without CA. **g**, Operational stability results of the devices with and without CA. **h**, A

comparison of the EQEs between our work and the previous reported results based on lead-free PeLEDs.

We then fabricated the Sn-PeLEDs with a conventional structure (Fig. 4a). The target Sn-PeLED showed electroluminescent spectra centered at ~630 nm under different voltages (Fig. 4b), and the luminance distribution is consistent with a Lambertian profile. The corresponding Commission Internationale de L'Eclairage (CIE) color coordinates are (0.69, 0.31) (Fig. 4c), demonstrating a high color-purity red emission. Compared with the reference device, the target Sn-PeLED had a narrower FWHM (24.9 nm) (Supplementary Fig. 12), indicating greater potential in the field of pure-red lighting and displays. Fig. 4d shows the current density (*J*)-voltage (*V*)-luminance (*L*) curves of the representative Sn-PeLEDs. The target devices attained a maximum EQE of 20.13%, which is considerably higher than that of the control Sn-PeLEDs (peak EQE of 4.37%) (Fig. 4e and Extended Data Fig. 8). A statistical distribution of EQEs of the Sn-PeLEDs is shown in Fig. 4f. The average EQE of the target Sn-PeLEDs was 15.9%, which is about 7-fold higher than that of the reference devices (2.37%). Noticeably, the turn-on voltage of the target device was 0.3 V lower than that of the pristine device, which is consistent with the enhanced luminance and EQE. These results unambiguously demonstrated a reduction of non-radiative recombination in the target Sn-PeLEDs. In addition, ultraviolet photoelectron spectroscopy measurements showed that the target Sn perovskite layer had better band alignment with both electron and hole transporting layers, favoring charge injection and transport, which was further validated by the space charge-limited current (SCLC) measurements (Supplementary Figs. 13 and 14). Operational stability tests were further conducted for the Sn-PeLEDs at a constant current density (initial luminance was 30 cd/m^2 in a N_2-filled glovebox). The target device demonstrated more than three-fold longer operating half-lifetime (T_{50}) than that of the reference (27.6 h versus 9.1 h) as shown in Fig. 4g, standing for one of best T_{50} results among lead-free PeLEDs. To highlight our work, we summarized the EQEs of Pb-free PeLEDs reported so far (Fig. 4h and Extended Data Table 1). The champion EQE achieved is fully comparable to those of Pb-based PeLEDs. We attribute the excellent optoelectronic performance and operational stability of the lead-free PeLEDs to reduced defect density and halide ion migration, enhanced exciton binding energy and suppressed nonradiative recombination.

In summary, integrating CA into two-dimensional TEA_2SnI_4 broke through the current performance bottleneck of Pb-free PeLEDs and allowed us to achieve an EQE over 20%. The polyfunctional character of CA led to the formation of well-oriented and highly-stable tautomeric CA complex that enable strong chemical coordination to Sn(II) with beneficial effects on crystallographic orientation and shelf stability of the Sn perovskite films yielding improved radiative recombination. Importantly, the cooperative coordination-induced electron localization of Sn(II) via CA di/trimeric surface complex is key for stabilizing Sn(II). Beyond solid-state electroluminescence, this fundamental advance could be broadly applicable to lead-free perovskite semiconductors for versatile applications.

References

1 Kim, J. S. *et al.* Ultra-bright, efficient and stable perovskite light-emitting diodes. *Nature* **611**, 688-694 (2022).

2 Jiang, Y. *et al.* Synthesis-on-substrate of quantum dot solids. *Nature* **612**, 679-684 (2022).

3 Cao, Y. *et al.* Perovskite light-emitting diodes based on spontaneously formed submicrometre-scale structures. *Nature* **562**, 249-253 (2018).

4 Lei, Y. *et al.* Perovskite superlattices with efficient carrier dynamics. *Nature* **608**, 317-323 (2022).
5 Luo, J. *et al.* Efficient and stable emission of warm-white light from lead-free halide double perovskites. *Nature* **563**, 541-545 (2018).
6 Ma, D. *et al.* Distribution control enables efficient reduced-dimensional perovskite LEDs. *Nature* **599**, 594-598 (2021).
7 Lin, K. *et al.* Perovskite light-emitting diodes with external quantum efficiency exceeding 20 per cent. *Nature* **562**, 245-248 (2018).
8 Hassan, Y. *et al.* Ligand-engineered bandgap stability in mixed-halide perovskite LEDs. *Nature* **591**, 72-77 (2021).
9 Chiba, T. *et al.* Anion-exchange red perovskite quantum dots with ammonium iodine salts for highly efficient light-emitting devices. *Nat. Photon.* **12**, 681-687 (2018).
10 Jeong, J. *et al.* Pseudo-halide anion engineering for α-$FAPbI_3$ perovskite solar cells. *Nature* **592**, 381-385 (2021).
11 Guo, B. *et al.* Ultrastable near-infrared perovskite light-emitting diodes. *Nat. Photo.* **16**, 637-643 (2022).
12 Kim, Y.-H. *et al.* Comprehensive defect suppression in perovskite nanocrystals for high-efficiency light-emitting diodes. *Nat. Photon.* **15**, 148-155 (2021).
13 Zhou, J. *et al.* Chemo-thermal surface dedoping for high-performance tin perovskite solar cells. *Matter* **5**, 683-693 (2022).
14 Jiang, X. *et al.* One-Step Synthesis of SnI_2·$(DMSO)_x$ Adducts for High-Performance Tin Perovskite Solar Cells. *J. Am. Chem. Soc.* **143**, 10970-10976 (2021).
15 Yu, B.-B. *et al.* Heterogeneous 2D/3D Tin-Halides Perovskite Solar Cells with Certified Conversion Efficiency Breaking 14%. *Adv. Mater.* **33**, 2102055 (2021).
16 Yuan, F. *et al.* Color-pure red light-emitting diodes based on two-dimensional lead-free perovskites. *Sci. Adv.* **6**, eabb0253 (2020).
17 Zhang, F. *et al.* Vapor-Assisted In Situ Recrystallization for Efficient Tin-Based Perovskite Light-Emitting Diodes. *Adv. Mater.* **34**, 2203180 (2022).
18 Lu, J. *et al.* Dendritic $CsSnI_3$ for Efficient and Flexible Near-Infrared Perovskite Light-Emitting Diodes. *Adv. Mater.* **33**, 2104414 (2021).
19 Heo, J.-M. *et al.* Bright Lead-Free Inorganic $CsSnBr_3$ Perovskite Light-Emitting Diodes. *ACS Energy Lett.* **7**, 2807-2815 (2022).
20 Liang, H. *et al.* High Color Purity Lead-Free Perovskite Light-Emitting Diodes via Sn Stabilization. *Adv. Sci.* **7**, 1903213 (2020).
21 Chen, M.-Y. *et al.* Strongly Coupled Tin-Halide Perovskites to Modulate Light Emission: Tunable 550–640 nm Light Emission (FWHM 36–80 nm) with a Quantum Yield of up to 6.4%. *Adv. Mater.* **30**, 1706592 (2018).
22 Cametti, G. *et al*. Role of lone-pair electron localization in temperature-induced phase transitions in mimetite. Acta Crystallogr. B Struct. Sci. Cryst. Eng. Mater **78**, 618-626 (2022).
23 Ye, T. *et al.* Localized Electron Density Engineering for Stabilized B-γ CsSnI3-Based Perovskite Solar Cells with Efficiencies >10%. *ACS Energy Lett.* **6**, 1480-1489 (2021).
24 Pérez-Manríquez, L. *et al.* Aromaticity in cyanuric acid. *J. Molec. Mod.***17**, 1311-1315 (2011).
25 Prabhaharan, M. *et al*. Density functional theory studies on molecular structure, vibrational spectra and electronic properties of cyanuric acid. Spect. Acta A: Mol. Biomol. Spect **138**, 711-722 (2015).
26 Zhang, J. *et al.* Understanding steric-charge-dependence of conjugated passivators on π-Pb^{2+} bond strength for efficient all-inorganic perovskite solar cells. *Chem. Eng. J.* **431**, 134230 (2022).

27 Pedireddi, V. *et al*. Investigation of some layered structures of cyanuric acid. *Tetrahedron* **58**, 2937-2941 (2002).
28 Falvello, L. *et al*. The Cyanurate Ribbon in Structural Coordination Chemistry: An Aggregate Structure That Persists across Different Coordination Environments and Structural Types. *J. Am. Chem. Soc.* **119**, 11894-11902 (1997).
29 Zhang, Q. *et al.* Stable Lead-Free Tin Halide Perovskite with Operational Stability >1200 h by Suppressing Tin(II) Oxidation. *Angew. Chem. Intern. Ed.* **61**, e202205463 (2022).
30 Zai, H. *et al.* Sandwiched electrode buffer for efficient and stable perovskite solar cells with dual back surface fields. *Joule* **5**, 2148-2163 (2021).
31 Liu, J. *et al.* Efficient and stable perovskite-silicon tandem solar cells through contact displacement by MgF_2. *Science* **377**, 302-306 (2022).
32 Jia, H. *et al.* Biuret Induced Tin-Anchoring and Crystallization-Regulating for Efficient Lead-Free Tin Halide Perovskite Light-Emitting Diodes. *Small* **18**, 2200036 (2022).
33 Wang, K. *et al.* Lead-Free Organic-Perovskite Hybrid Quantum Wells for Highly Stable Light-Emitting Diodes. *ACS Nano* **15**, 6316-6325 (2021).
34 Gao, C. *et al.* Multifunctional Naphthol Sulfonic Salt Incorporated in Lead-Free 2D Tin Halide Perovskite for Red Light-Emitting Diodes. *ACS Photonics* **7**, 1915-1922 (2020).
35 Liao, Y. *et al*. Two-dimensional tin perovskite nanoplate for pure red light-emitting diodes. *J. Phy. D: App. Phy.* **53**, 414005 (2020).
36 Ma, J.-Y. *et al*. Temperature-Dependent Local Electrical Properties of Organic–Inorganic Halide Perovskites: In Situ KPFM and c-AFM Investigation. *ACS Appl. Mater. & Inter.* **11**, 21627-21633 (2019).
37 Ren, Z. *et al*. Simultaneous Low-Order Phase Suppression and Defect Passivation for Efficient and Stable Blue Light-Emitting Diodes. *ACS Energy Lett.* **5**, 2569-2579 (2020).
38 Su, Y. *et al*. Acetic Acid-Assisted Synergistic Modulation of Crystallization Kinetics and Inhibition of Sn^{2+} Oxidation in Tin-Based Perovskite Solar Cells. *Adv. Funct.l Mater.***32**, 2109631 (2022).
39 Zou, W. *et al.* Minimising efficiency roll-off in high-brightness perovskite light-emitting diodes. *Nat. Commun.* **9**, 608 (2018).
40 Luo, Y. *et al.* A Multifunctional Ionic Liquid Additive Enabling Stable and Efficient Perovskite Light-Emitting Diodes. *Small* **18**, 2200498 (2022).
41 Zhang, T. *et al.* Regulation of the luminescence mechanism of two-dimensional tin halide perovskites. *Nat. Commun.* **13**, 60 (2022).

Data availability: The data that support the findings of this study are available from the corresponding authors.

Competing interests: The authors declare no competing interests.

Acknowledgments: This work was partly supported from the National Natural Science Foundation of China (Grant No. 51972137, 12175298 and 62174104), the Science and Technology Planning Project of Jilin Province (Grant No. 20190201306JC) and the start-up funding of Jilin University. Y.Y. acknowledges the financial support from Shanghai Municipal Commission for Science and Technology (No. 20ZR1464100). U. R. acknowledges the Swiss National Science Foundation Grant No. 200020-185092 for funding as well as computational resources from the Swiss National Computing Centre CSCS. M.G. acknowledges financial support from the European Union's Horizon 2020 research and innovation program under grant agreement number 881603.We thank the staff of beamlines BL17B1, BL19U1 and BL19U2 at SSRF for providing the beam time and User Experiment Assist System of SSRF for their help.

Author contributions: We thank Mingguang Yao and Jiajia Ning for discussions, and Gang Chen for TA measurements. H.L. X.Y. N.W. and M.G. supervised this project. N.W. conceived the idea. D.H. and J.W. fabricated and characterized the PeLED devices. D.H., J.W. and Z.Z. fabricated the perovskite films for experimental measurements. L.A., B.Z., H.J., I.M-L., V.C., L.P., S.M.Z. conducted the simulations with U.R.'s guidance. J.Z. performed the film morphology measurements. J.D. and D.H. conducted XRD and temperature-dependent steady-state PL spectra measurements. Y.Y. and L.K. conducted the GIWAXS measurements. D.H., B.W. and Y.Y. analyzed the results of GIWAXS and TA measurements. N.W., H.L., X.Y., Y.Y., D.H., J.W., Z.Z., I.M., V.C., L.A., L.P., S.M.Z., U.R. and M.G. prepared and polished the manuscript. All authors discussed the results and commented on the paper.

Methods

Materials

Tin (II) iodine (SnI_2, Advanced Election Technology Co., Ltd), toluene (Sigma Aldrich). Silver (Ag, Alfa Aesar). Aluminum (Al, Alfa Aesar), tin power (Alfa Aesar), lithium fluoride (LiF) (Aladdin), rubidium iodide (RbI, Sigma Aldrich). Patterned indium tin oxide (ITO) (~15 Ω/sq) coated glasses were purchased from Jinge-Solar Tech. 2-thiopheneethylamine iodine (TEAI), poly(3,4-ethylenedioxythiophene)/poly(styrenesulfonate) (PEDOT:PSS, Heraeus Clevios™ AI 4083) and 2,2',2"-benzene-1,3,5-triyltris(1-phenyl-1H-benzimidazole) (TPBi) were purchased from Xi'an Polymer Light Technology Corp. Molybdenum trioxide (MoO_3), N, N-dimethylformamide (DMF), dimethyl sulfoxide (DMSO) and cyanuric acid (CA) were purchased from Innochem. polymethyl methacrylate (PMMA, Sigma Aldrich), KBr (Aladdin). All these materials were used without further purification.

Preparation of TEA_2SnI_4 perovskite films

For tin perovskite precursor solution (0.2 M), TEAI and SnI_2 with a molar ratio of 2.2:1 were dissolved in anhydrous DMF/DMSO (4:1 v/v) solution, and RbI (6 mg/mL) and tin power (50 mg/mL) were added. The precursor solution was stirred in a N_2-filled glovebox (H_2O and O_2, < 0.01 ppm) overnight at 50 °C and then filtered with a 0.22 μm polytetrafluoroethylene (PTFE) filter before use. The tin perovskite films were spin-coated via one-step process, 50 μL perovskite precursor (concentrations of 0%, 2%, 5% and 8% CA) was dropped onto the PEDOT: PSS substrates at 5000 rpm for 55 s, and then 200 μL anhydrous toluene was dropped onto the substrate at 10 s after spin-coating. Finally, the obtained perovskite thin films were annealed at 100 °C for 10 min inside glovebox. The corresponding films are denoted as pristine, with 2% CA, with 5% CA, and with 8% CA, respectively. In this text, with 5% CA is abbreviated to 'with CA'.

Device fabrication

The ITO-coated glass substrates were ultrasonically cleaned for 20 minutes with detergent, deionized water, acetone, and isopropyl alcohol, respectively. And then the cleaned ITO-coated glass substrates were treated with ultraviolet-ozone for 20 min. Modified PEDOT: PSS solution was prepared by mixing PEDOT: PSS solution with deionized water with a volume ratio of 7:3. Then, PEDOT: PSS solution was spin-coated onto the treated-ITO substrate at 4000 rpm for 30 s and then the substrates were annealed in air at 150 ℃ for 20 min. After that, the substrates were transferred into a N_2-filled glovebox for 20-min annealing (150 ℃) again. After spin coating the tin perovskite films as described above, the substrates were transferred into a vacuum thermal evaporator. Finally, 30 nm TPBi, 1 nm LiF and 100 nm Al electrode were deposited in sequence, under a high vacuum < 5×10^{-4} Pa. The effective area was defined using masks as 0.06 cm^2.

Characterizations

Steady-state photoluminescence (PL) (Omni-λ 300 Monochromator/Spectrometer, Zolix) and TRPL (Horiba DeltaPro fluorescence lifetime system) measurements were performed with Sn perovskite films spin-coated on quartz substrates. The TRPL curves were fitted with biexponential equations:

$$I = A + B_1 e^{-t/\tau_1} + B_2 e^{-t/\tau_2} \quad (1)$$

where I is the normalized PL intensity, A, B_1, and B_2 are the decay amplitudes, and $A + B_1 + B_2 = 1$. τ_1 and τ_2 correspond to the lifetime constants of fast and slow components, respectively. The $\tau_{average}$ is given by the equation below:

$$\tau_{average} = B_1\tau_1 + B_2\tau_2 \quad (2)$$

For temperature-dependent PL measurements, Sn perovskite films prepared on quartz substrates were mounted in a cryostat (Janis ST-100) and cooled by liquid nitrogen. The samples were excited by a continuous wave laser at an excitation wavelength of 400 nm (power density of 2 μJ cm^{-2}, and 20 K intervals). X-ray diffraction (XRD) results were collected from Rigaku Smart Lab X-ray diffractometer with Cu Kα radiation (λ = 1.54050 Å). The GIWAXS was performed at BL17B1 and BL19U2 beamline of SSRF using the X-ray energy of 10KeV. Two-dimensional patterns of Sn perovskite films on silicon wafer substrates were acquired by a PLATUS 2M detector mounted vertically at a distance of ~240 mm from the sample with a grazing incidence angle of 0.2º~0.4 º and an exposure time of 20 s. Electrochemical impedance spectroscopy (EIS) experiments of the Sn-PeLED devices were carried out with an electrochemical workstation (CHI660C, CH Instruments). All Sn-PeLED devices were measured in a N_2-filled glovebox using Keithley 2400 and Konica Minolta CS-200. Electroluminescence characteristics were recorded with a Flame spectrometer and an integrating sphere (Ocean Optic). The light distribution was measured by using a Konica Minolta CS-200 detector, coordinating with various angles from 0º to 90º. Morphology and energy dispersive X-ray spectroscopy (EDS) of the Sn perovskite films were characterized by scanning electron microscope (SEM) (Hitachi S-4800). AFM measurements were performed using a Bruker Nano ICON2-SYS microscope (Germany). Kelvin probe force microscopy (KPFM) potential and topographic mappings were obtained using a Digital Instruments Multimode AFM (Veeco Metrology Group), and the used tin perovskite films were deposited on ITO/PEDOT:PSS substrate. The optical properties of the tin perovskite films were measured using UV-Vis absorption spectroscopy (shimadzu UV-vis-NIR spectrometer (UV-2600i)). Transient-absorption spectroscopy (TA) measurements were performed using a commercial setup (Helios, Ultrafast Systems). The wavelength and the energy density of pump pulse were 400 nm and 8 μJ cm^{-2}, respectively. The perovskite films for TA characterization were fabricated on quartz substrates, spin-coating a layer of PMMA with a concentration of 20 mg/ml on the perovskite surface. X-ray photoelectron spectroscopy (XPS) and ultraviolet photoelectron spectroscopy (UPS) spectra were obtained with Hitachi Regulus 8100. The excitation-intensity-dependent photoluminescence quantum yields (PLQYs) were measured by a homemade instrument combining a 405 nm laser, spectrometer, and integrating sphere. Nuclear magnetic resonance (NMR), ^{1}H NMR and ^{13}C NMR spectra were recorded using Bruker AVIII 500MHz FT-NMR. Fourier Transform Infrared (FTIR) Spectroscopy was tested with Thermo Scientific Nicolet Is10 Instrument, the powder scraped from the perovskite films was mixed with dry KBr powder and ground directly, pressure is applied to press the powder into transparent sheet for testing. The electrostatic potentials (ESP) are calculated using Gaussview software using a self-consistent field density matrix.

Defect density and carrier mobility calculations

The defect density can be deduced from the onset voltage of the trap-filled limit region (V_{TFL}), as shown in equation (3). The carrier mobility of the Sn perovskite films was obtained by SCLC method using the Mott-Gurney law equation (4):

$$N_t = 2\varepsilon_0\varepsilon_r V_{TFL}/qL^2 \quad (3)$$

$$J = 9/8\mu\varepsilon_0\varepsilon_r {V_{TFL}}^2/L^3 \quad (4)$$

where L is the thickness of perovskite film, ε_r is the relative dielectric constant, ε_0 is the vacuum permittivity, q is the charge constant, and μ is the carrier mobility. The hole-only device with an architecture of ITO/PEDOT:PSS/perovskite/MoO_3 (30 nm)/Ag (100 nm) was used. The

electron-only device with a structure of ITO/TPBi (30 nm)/perovskite/TPBi (30 nm)/LiF (3 nm)/Ag (100 nm) was used.

Stability measurement

LED stability was measured in a N_2-filled glovebox at room temperature without encapsulation under dark condition. The devices were driven by a Keithley 2400 source meter at a constant current and the luminance was measured using a Konica Minolta CS-200 with an initial luminance of 30 cd m^{-2}.

Arrhenius equation

$$I(\mathrm{T}) = I_0/(1 + Ae^{-E_b/k_B T}) \qquad (5)$$

in which I_0 is the PL intensity at 0 K, k_B is the Boltzmann constant and E_b is the exciton binding energy.

System model

The structure of TEA_2SnI_4 was initially built by combining the inorganic framework of FA_2SnI_4 (FA is formamidinium) with the TEA cations (instead of FA). The distance between the Pb-I layers was initially set to 15.45 Å, as obtained from the XRD measurements. To model the surface, we built a slab containing two inorganic layers (Extended Data Fig 2) and a vacuum space of 17 Å. For the ab-initio molecular dynamics simulations, this model was expanded to a 4×3×1 supercell.

Static Density Functional Theory calculations

The structural and electronic properties of tin perovskite surfaces have been investigated by first-principles calculations based on density functional theory (DFT) as implemented in the Vienna ab initio simulation package (VASP)[42,43] The standard frozen-core projector augmented wave (PAW) method was utilized to describe the interactions between ions and electrons. Exchange-correlation effects were included by means of the generalized gradient approximation (GGA) of Perdew-Burke-Ernzerhof (PBE) functional[44]. The kinetic energy cutoff was set at 400 eV for the plane-wave expansion. The Monkhorst-Pack k-point grid with resolution of 0.2 $Å^{-1}$ was selected to sample the reciprocal space for the calculated systems[45] . A vacuum space of 20 Å was set between adjacent images to avoid any fictitious interactions. Dipole corrections (IDIPOL = 3) were employed to correct for the slab-to-slab dipole interactions along the surface normal direction. Grimme's dispersion correction scheme combined with Becke-Johnson damping was considered to correct for van der Waals interactions[46]. The bottom layers were fixed at the bulk crystal geometry[47]. The geometry optimizations were performed with a convergence criterion of 1.0×10^{-6} eV in energy and 0.005 eV/Å in forces. Calculations of the capture coefficient calculation were based on previous literature[48,49]. Nonradiative recombination coefficient B, which is defined as $B = N_{def} A$, where N_{def} is the defect density from being obtained single carrier devices, A is nonradiative recombination capture coefficient.

Ab-initio molecular dynamics

Born-Oppenheimer ab-initio (DFT-based) molecular dynamics simulations with a mixed Gaussian and plane wave (GPW) basis as implemented in the CP2K package[50-53] were performed to investigate the interaction between the molecules and the perovskite surface. Valence electrons were expanded in a double-ζ Gaussian basis set with polarization functions (DZVP)[54]. The energy cutoff for the electron density expansion in the GPW method was 400 Ry. The temperature was controlled by the velocity rescaling thermostat of Bussi *et al*.[55] with a time constant of 0.5 fs. All AIMD simulations were performed at the Γ-point. The lattice

parameters of the triclinic simulation box were allowed to relax for 2 ps in the isothermal-isobaric ensemble (NPT) with P = 1 atm. The system was then equilibrated over 5 ps in the NVT ensemble using the supercell volume obtained by the NPT simulation; 25 ps of simulation runs were used to estimate interaction patterns between the molecules and the surface. Vibrational power spectra are computed as the Fourier transform of the autocorrelation function of the atomic velocities. Three CA concentrations (CA molecules relative to Sn species, 4.16%, 8.33% and 12.5%) and two different starting scenarios (pure keto and pure enol CA isomers) were considered in the simulations (Extended Data Fig 2). Simulations show that pure keto isomer cannot be adsorbed stably on the Sn perovskite surface at any CA concentration.

42. Kresse, G. *et al*. Efficiency of ab-initio total energy calculations for metals and semiconductors using a plane-wave basis set. *Phys. Rev. B* **47** (1993).
43. Kresse, G. *et al*. From ultrasoft pseudopotentials to the projector augmented-wave method. *Phys. Rev. B* **59**, 1758-1775 (1999).
44. Blöchl, P. E. Projector augmented-wave method. *Phys. Rev. B* **50**, 17953-17979 (1994).
45. Perdew, J. P. *et al*. Generalized Gradient Approximation Made Simple. *Phys. Rev. Lett.* **77**, 3865-3868 (1996).
46. Pack, J. D. *et al*. "Special points for Brillouin-zone integrations"-a reply. *Phys. Rev. B* **16**, 1748-1749 (1977).
47. Grimme, S. *et al.* Semiempirical GGA-type density functional constructed with a long-range dispersion correction. *J. Comput. Chem.* **27**, 1787-1799 (2006).
48. Turiansky, M. E. *et al.* Nonrad: Computing nonradiative capture coefficients from first principles. *Comput. Phy. Commun.* **267**, 108056 (2021).
49. Perdew, J. P. *et al.* Restoring the Density-Gradient Expansion for Exchange in Solids and Surfaces. *Phys. Rev. Lett.* **100**, 136406 (2008).
50. Alkauskas, A. *et al.* First-principles theory of nonradiative carrier capture via multiphonon emission. *Phys. Rev. B* **90**, 075202 (2014).
51. Kresse, G. *et al*. Ab initio molecular-dynamics simulation of the liquid-metal-amorphous-semiconductor transition in germanium. *Phys. Rev. B* **49**, 14251-14269 (1994).
52. Grimme, S. *et al*. A consistent and accurate ab initio parametrization of density functional dispersion correction (DFT-D) for the 94 elements H-Pu. *J. Chem. Phys.* **132**, 154104 (2010).
53. Tang, H. *et al.* Plasmonic hot electrons for sensing, photodetection, and solar energy applications: A perspective. *J. Chem. Phys.* **152**, 220901 (2020).
54. Fletcher, R. E. *et al.* Violations of Löwenstein's rule in zeolites. *Chem. Sci.* **8**, 7483-7491 (2017).
55. Bussi, G. *et al*. Canonical sampling through velocity rescaling. *J. Chem. Phys.* **126**, 014101 (2007).

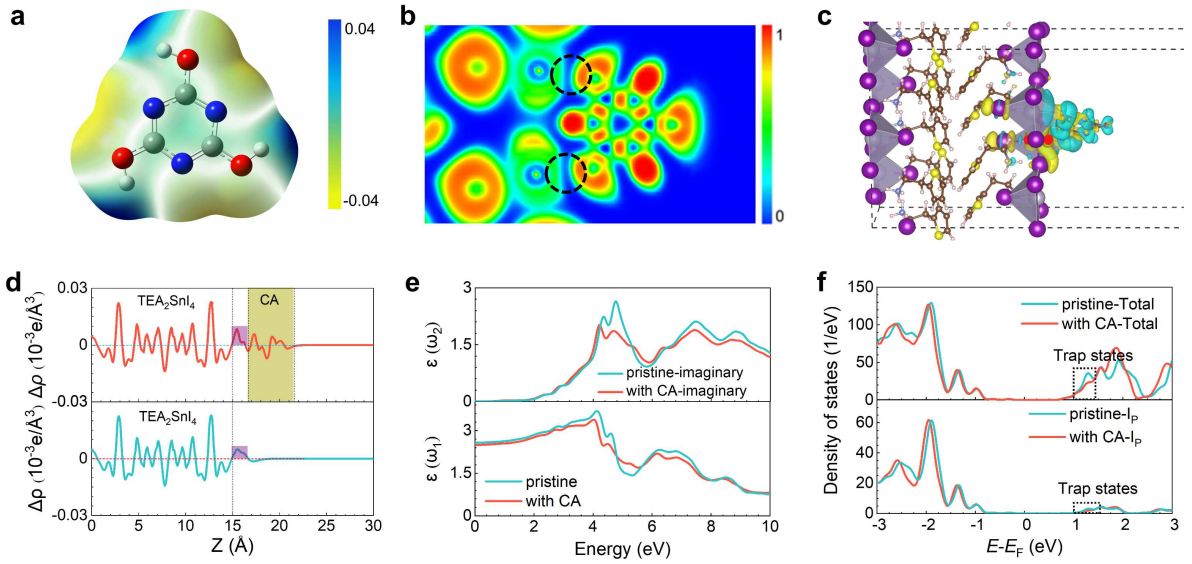

Extended Data Fig. 1 | Density functional theory study. a, Calculated electrostatic potential distribution for enol form of the CA molecule. **b**, ELF image for the triketo CA-treated perovskite. **c**, Charge density difference between the tin perovskite and triketo CA. Obtained in systems with an iodide vacancy. **d**, Planar-averaged charge density difference of the pristine and the Sn perovskite with CA. **e**, Dielectric coefficients of the Sn perovskites with and without CA along the Z-axis. **f**, Density of states for the pristine (blue) and the CA-treated perovskite (red) with a surface iodide vacancy.

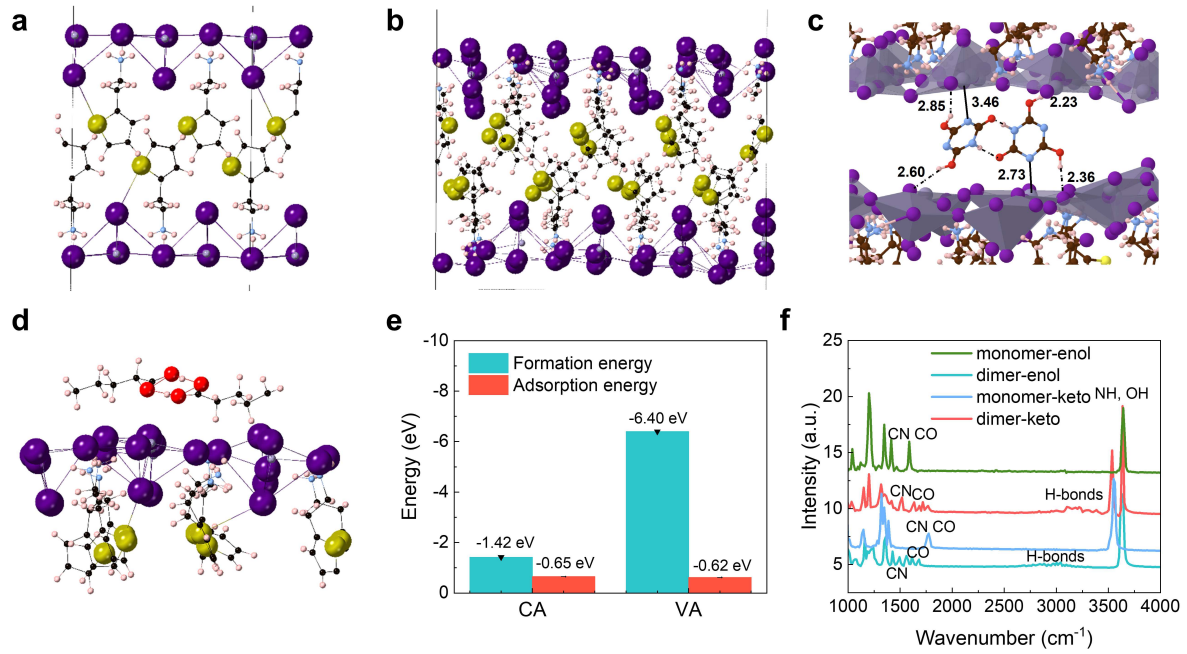

Extended Data Fig. 2 | Configuration and FTIR studies. a, **b**, Built slab containing two inorganic layers (**a**) and a vacuum space of 17 Å. For the ab-initio molecular dynamics simulations, this model was expanded to a 4×3×1 supercell (**b**). Color code: Sn in grey, I in purple, S in yellow, C in black, H in pink, O in red, N in blue. **c**, AIMD snapshoot of a stable dimer at a perovskite grain boundary. The distances are in Å. Color code: Sn in grey, I in purple, S in yellow, C in black, H in pink, O in red, N in blue. **d**, Valeric acid dimer on top of a pristine TEA_2SnI_4 surface. The protons are shared between two oxygens with distances of 1.0 Å and 1.6 Å. Valeric acid only contains one functional group - thus if the carboxylic acid group is used to form dimers, the molecule can no longer bind to the perovskite surface, as observed with ab initio MD simulations. **e**, Dimer formation energies (blue) and adsorption energies (red) for CA and valeric acid (VA). **f**, Vibrational power spectra of the CA keto and enol monomers and dimers in gas phase. The mixed enol-keto form can also explain the observed CO stretch in FTIR. This figure shows the vibrational power spectra of the gas phase molecules of monomers and dimers of the pure keto and pure enol CA form. In the monomeric form, the CN and CO modes overlap at 1587 cm^{-1} and 1775 cm^{-1} for the enol and keto forms, respectively. Upon dimerization, these peaks split into three components with the CO contribution blue shifted compared to the CN one. From these results we can conclude that the experimental spectra contain contributions from mixed keto/enol dimers. Furthermore, Fig. 1 shows the computed vibrational power spectra of the most stable trimer configuration in vacuum and adsorbed on the perovskite surface. When the trimer is adsorbed on the surface, a blue shift of 25 cm^{-1} and 15 cm^{-1} is reported for CN and CO modes, respectively, in agreement with the experimental data. Another clear signature that CA adsorbs in the form of trimers and/or dimers is the peak around 3000~3300 cm^{-1} due to OH and NH groups involved in H-bond interactions (CO-HNC); indeed, this kind of peaks are not present for monomers.

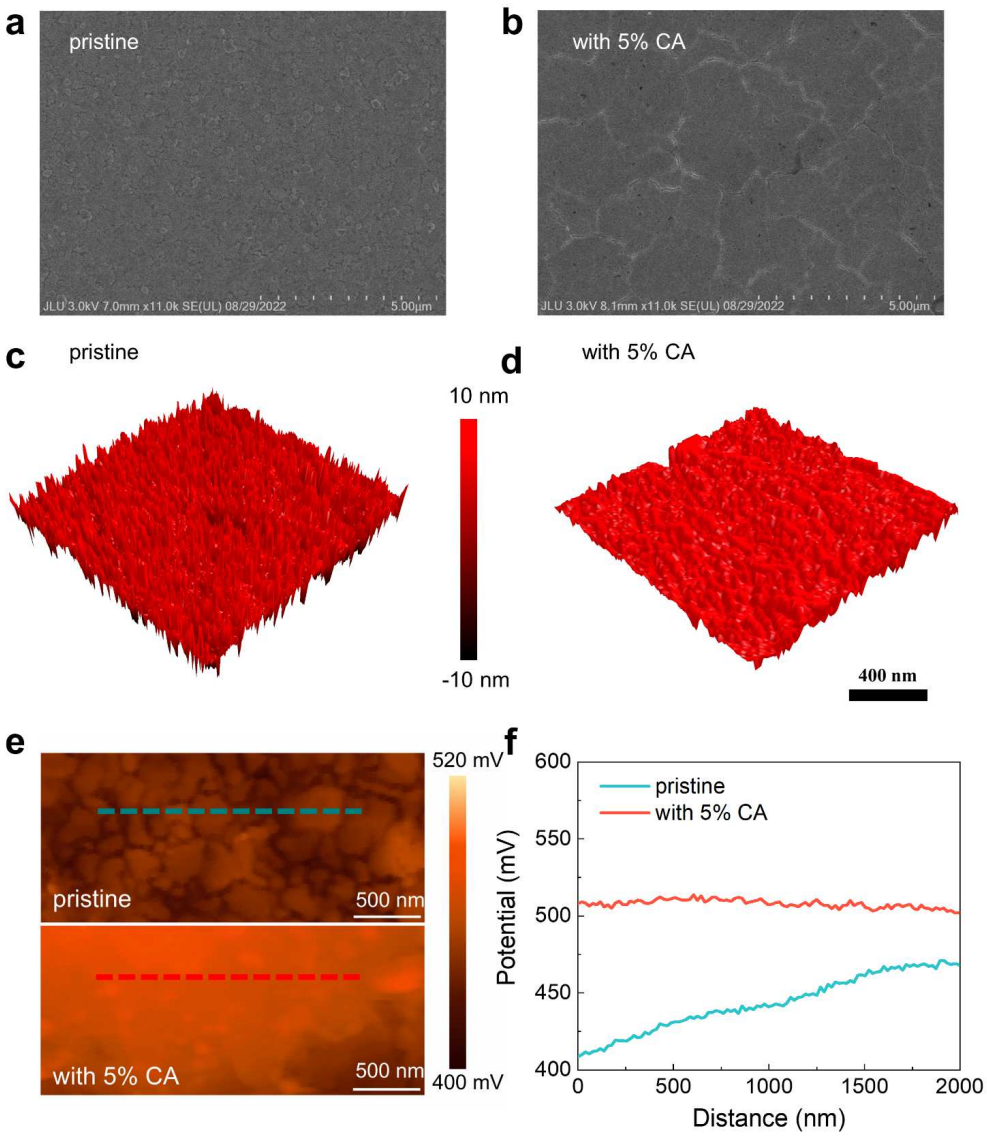

Extended Data Fig. 3 | Morphological characteristics. a, **b**, SEM images of the perovskite films without (**a**) and with 5% CA (**b**). **c**, **d**, AFM images of the pristine (**c**) and the 5% CA-treated sample (**d**). **e**, KPFM measurements for the pristine and the CA-treated sample. **f**, Linear potential profiles for the pristine and the CA-treated sample.

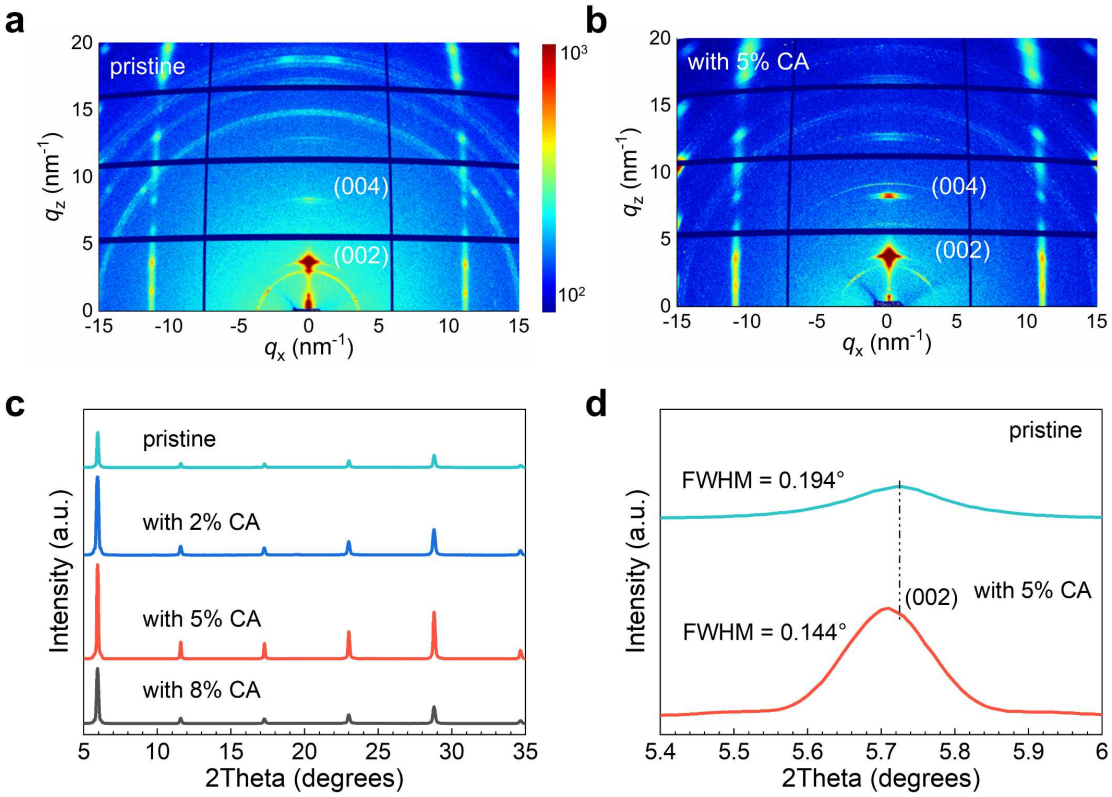

Extended Data Fig. 4 | Crystal structure of TEA_2SnI_4 films. a, **b**, GIWAXS images of TEA_2SnI_4 perovskite films without (**a**) and with 5% CA (**b**). **c**, XRD patterns of the pristine and the samples with 2%, 5% and 8% CA. **d**, Comparison of (002) peak for the samples with and without 5% CA.

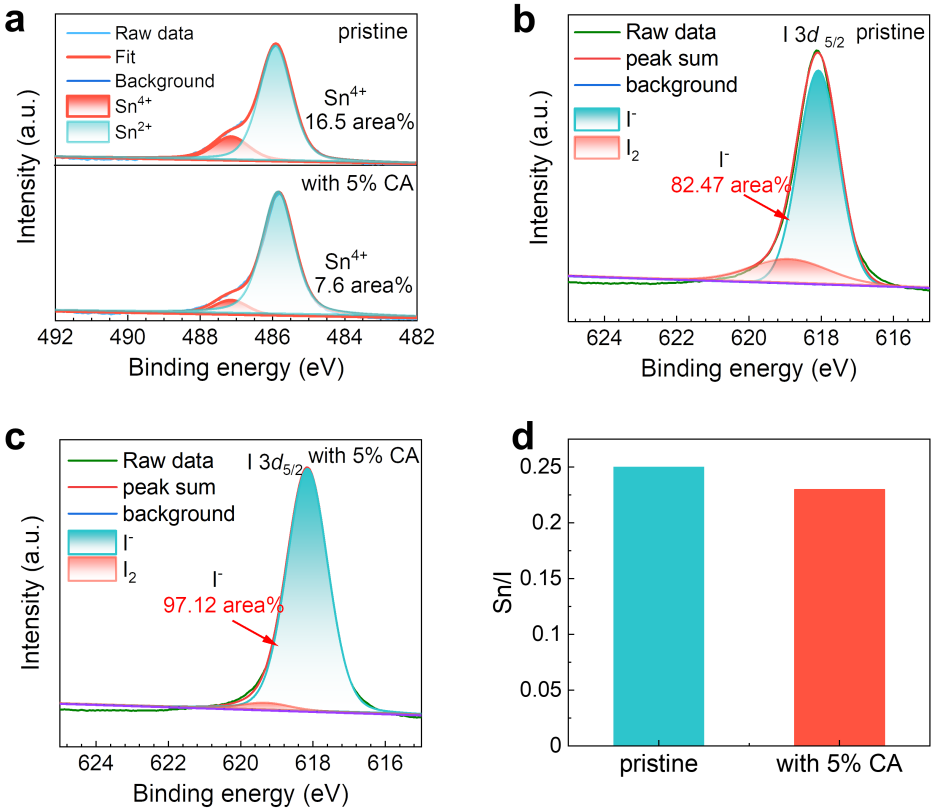

Extended Data Fig. 5 | XPS analysis of TEA_2SnI_4 films. a, XPS spectra of Sn 3*d* for the pristine and the CA-treated TEA_2SnI_4. **b**, **c**, XPS results of I 3*d* spectra for the tin perovskite films without (**b**) and with 5% CA (**c**). **d**, Ratios of Sn versus I from the XPS spectra for the tin perovskite samples with and without CA.

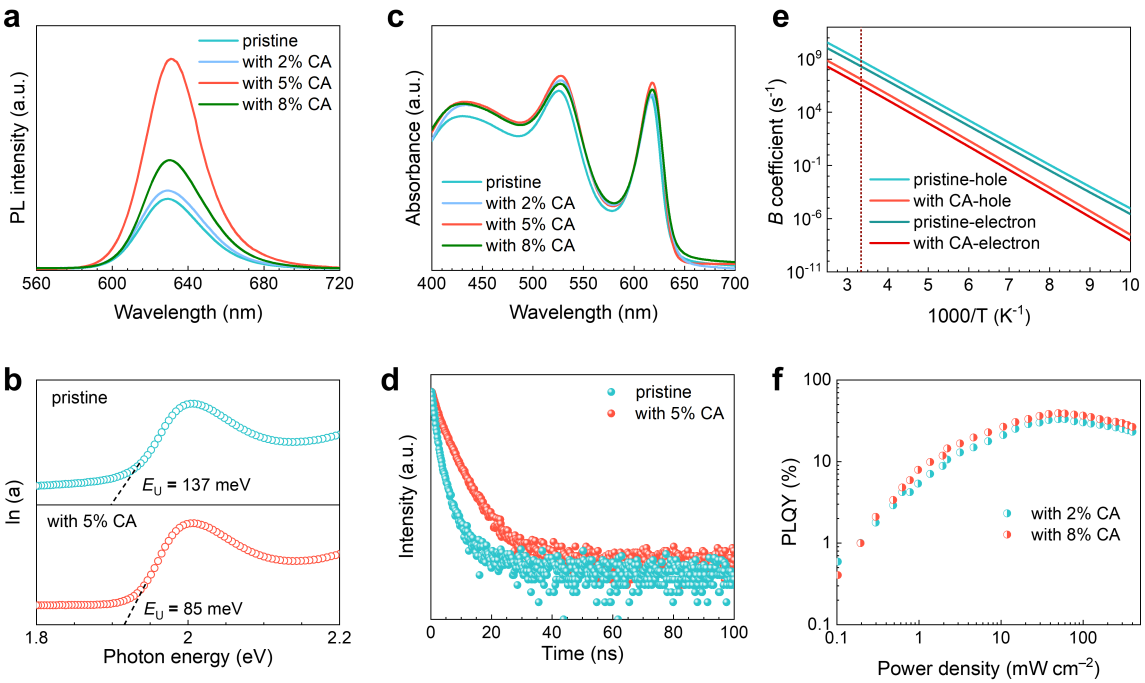

Extended Data Fig. 6 | Optical properties of the Sn perovskite films. a, PL spectra of the Sn perovskite films with various CA content. **b**, Logarithm curves of absorption coefficient (α) versus photon energy, the E_U for the pristine and the treated sample are estimated. **c**, Visible absorption spectra of the Sn perovskite films with various CA content. **d**, TRPL spectra of the TEA_2SnI_4 films prepared with and without 5% CA. **e**, Nonradiative recombination coefficients B for the single-carrier devices with and without CA treatment, the dashed line indicates the condition of room temperature. **f**, Excitation-intensity-dependent PLQYs of the perovskite films with different CA content.

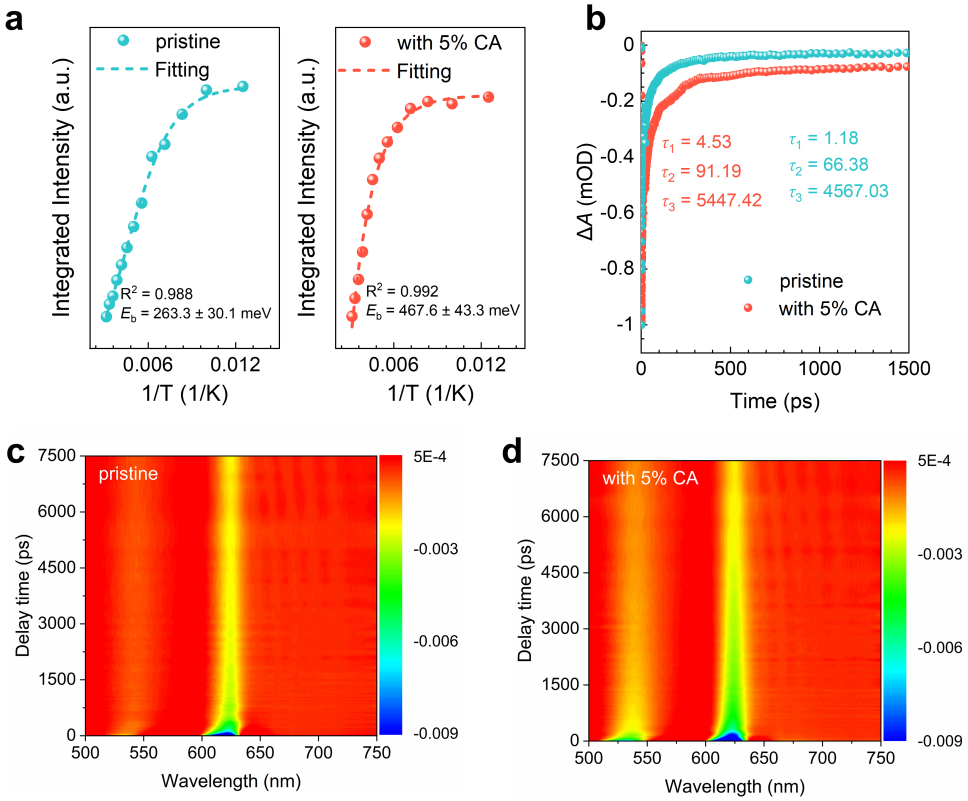

Extended Data Fig. 7 | Photophysical characterization of TEA_2SnI_4 films. a, The fitted curves of the integrated PL intensity as a function of 1/T for the perovskites with and without CA. **b**, Kinetic traces at a probing wavelength of 615 nm for the Sn perovskite films with and without CA. **c**, **d**, Pseudo-color maps of femtosecond-transient absorption spectra of the pristine (**c**) and the sample with 5% CA (**d**) under an excitation wavelength of 400 nm.

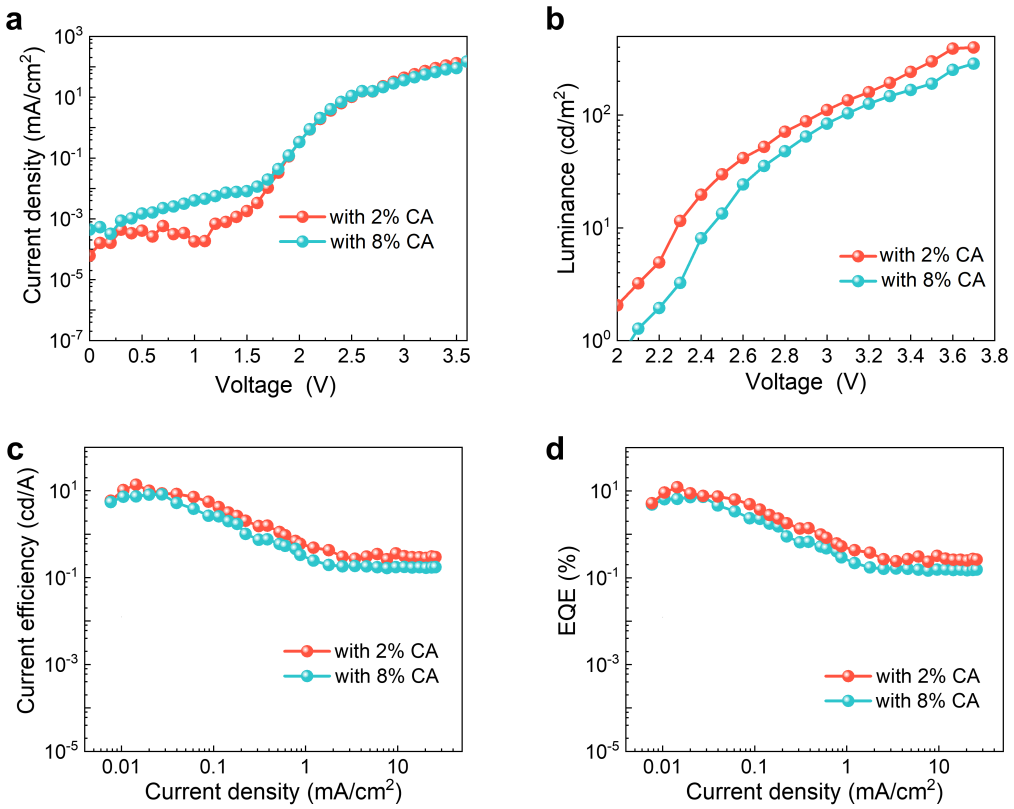

Extended Data Fig. 8 | Device characterization. a-d, Device performance for the Sn-PeLEDs with 2% and 8% CA: (**a**) *J-V,* (**b**) *L-V,* (**c**) *CE-J*, and (**d**) *EQE-J* curves.

Extended Data Table 1 | Summary of device performance for recently reported lead-free PeLEDs.

No.	Materials	λ_{EL} (nm)	FWHM (nm)	EQE (%)	References
1	$CsSnI_3$	950	~80	3.8	*Adv. Mater.* **28**, 8029-8036 (2016)
2	$CH_3NH_3SnI_3$	954	~60	0.7	*ACS Nano* **14**, 4475–4486 (2020)
3	$CsSnBr_3$	672	54	0.3	*Phys. Status Solidi RRL*, **12**, 1800090 (2018)
4	$MASnI_3$	901	~80	0.9	*Adv. Mater.* **31**, 1806105 (2019)
5	$(PEAI)_{3.5}(CsI)_5(SnI_2)_{4.5}$	920	~70	3	*J. Phys. Chem. Lett.* **10**, 453 (2019)
6	$CsSnBr_3$	674	~45	0.2	*J. Lumin.* **226**, 117493 (2020)
7	$(PEA)_2SnI_4$	633	24	0.30	*Adv. Sci.* **7**, 1903213 (2020)
8	PEA_2SnI_4	632	~30	0.72	*ACS Photonics* **7**, 1915-1922 (2020)
9	$(PEA)_2SnI_4$	630	29	0.52	*J. Phys. D: Appl. Phys.* **53**, 414005 (2020)
10	$(PEA)_2SnI_4$	633	~36	1.48	*J. Mater. Chem. C* **9**, 12079-12085 (2021)
11	$(PEA)_2SnI_4$	632	21	5	*Sci. Adv.* **6**, eabb0253 (2020)
12	$(C_{18}H_{35}NH_3)_2SnBr_4$	625	162	0.1	*ACS Energy Lett.* **4**, 242-248 (2019)
13	$(BTm)_2SnI_4$	627	27.8	3.33	*ACS Nano* **15**, 6316-6325 (2021)
14	$(TEA)_2SnI_4$	638	32	0.62	*J. Phys. Chem. Lett.* **11**, 1120-1127 (2020)
15	$(TEA)_2SnI_4$	638	32	1.37	*Small* **18**, 2200036 (2022)
16	$CsSnBr_3$	674	~40	-	*ACS Energy Lett.* **7**, 2807-2815 (2022)
17	$CsSnI_3$	932	~48	5.4	*Adv. Mater.* **33**, 2104414 (2021)
18	$PEAI\text{-}FASnI_3$	866	~48	5.3	*Adv. Mater.* **34**, 2203180 (2022)
19	**$(TEA)_2SnI_4$**	**630**	**24.9**	**20.13**	**This work**
20	$Cs_3Cu_2I_5$	438	58	0.1	*J. Semicond.* **41**, 052204 (2020)
21	$Cs_3Cu_2I_5$	445	58	1.1	*Nano Lett.* **20**, 3568 (2020)
22	$CsCu_2I_3$	560	180	0.02	*ACS Appl. Mater. Inter.* **12**, 52967 (2020)
23	$CsCu_2I_3$	550	~120	0.2	*ACS Nano.***14**, 4475 (2020)
24	$CsCu_2I_3$	568	~120	0.2	*ACS Energy Lett.* **6**, 2584–2593 (2021)
25	$Cs_3Cu_2I_5$:$CsCu_2I_3$	565	120	3.1	*Nat. Commun.* **12**, 1421 (2021)
26	$TmPyPB\text{-}CsCu_2I_3$	578	~140	7.4	*ACS Energy Lett.* **6**, 2584–2593 (2021)
27	$Cs_3Sb_2Br_9$	408	~60	0.2	*ACS Energy Lett.* **5**, 385 (2019)
28	$CsEuBr_3$	448	~30	6.5	*Adv. Mater.* **33**, 2101903 (2021)
29	Cs_3CeBr_6	421	~70	0.5	*ACS Energy Lett.* **6**, 4245–4254 (2021)
30	$Cs_3CeBr_xI_{6-x}$	430	-	3.5	*Sci. Adv.* **8,** *eabq2148* (2022)
31	$(ABI)_4MnBr_6$	627	45	9.8	*Adv. Funct. Mater.* **31**, 2100855 (2021)

λ_{EL} is the peak wavelength of electroluminescent PeLEDs.

Supplementary Files

This is a list of supplementary files associated with this preprint. Click to download.

- NatureSupplementaryInformation.pdf